Check for updates

View Article Online
View Journal

Journal of
Materials Chemistry C

Materials for optical, magnetic and electronic devices

Accepted Manuscript

This article can be cited before page numbers have been issued, to do this please use: C. Panagopoulou, P. Bousoulas, A. Kalafatis, S. Orfanoudakis, C. Tsioustas, A. Banis, P. Tsipas, A. G. Kontos, T. Stergiopoulos and D. Tsoukalas, *J. Mater. Chem. C*, 2026, DOI: 10.1039/D5TC03487F.

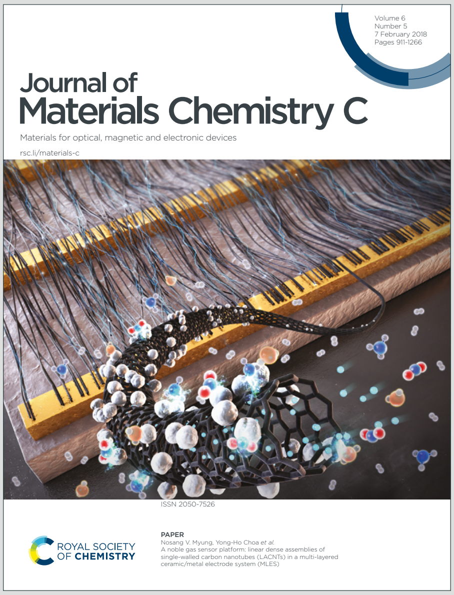

Volume 6
Number 5
7 February 2018
Pages 911-1266

Journal of
Materials Chemistry C

Materials for optical, magnetic and electronic devices

rsc.li/materials-c

ISSN 2050-7526

ROYAL SOCIETY
OF CHEMISTRY

PAPER
Nosang V. Myung, Yong-Ho Choa *et al.*
A noble gas sensor platform: linear dense assemblies of single-walled carbon nanotubes (LACNTs) in a multi-layered ceramic/metal electrode system (MLES)

This is an Accepted Manuscript, which has been through the Royal Society of Chemistry peer review process and has been accepted for publication.

Accepted Manuscripts are published online shortly after acceptance, before technical editing, formatting and proof reading. Using this free service, authors can make their results available to the community, in citable form, before we publish the edited article. We will replace this Accepted Manuscript with the edited and formatted Advance Article as soon as it is available.

You can find more information about Accepted Manuscripts in the Information for Authors.

Please note that technical editing may introduce minor changes to the text and/or graphics, which may alter content. The journal's standard Terms & Conditions and the Ethical guidelines still apply. In no event shall the Royal Society of Chemistry be held responsible for any errors or omissions in this Accepted Manuscript or any consequences arising from the use of any information it contains.

ROYAL SOCIETY
OF CHEMISTRY

rsc.li/materials-c

View Article Online
DOI: 10.1039/D5TC03487F

COMMUNICATION

Optoelectronic inhibitory synapses in the visible range from PbS nanocrystal arrays

Received 00th September 20xx,
Accepted 00th September 20xx

DOI: 10.1039/x0xx00000x

Chrysi Panagopoulou*[a], Panagiotis Bousoulas[a], Apostolos Kalafatis[b,c], Spyros Orfanoudakis[a,b], Charalampos Tsioustas[a], Alexandros Banis[b], Polychronis Tsipas[b], Athanassios G. Kontos[a,b], Thomas Stergiopoulos*[b] and Dimitris Tsoukalas [a]

Optoelectronic inhibitory synapses play critical roles in modulating neural activity and maintaining the balance between excitation and inhibition within artificial neural circuits. However, most reported devices fail to properly emulate depression-related synaptic functions under optical stimulation. In this work, we demonstrate an optoelectronic inhibitory synaptic device based on lead sulfide (PbS) nanocrystals capped with iodide ligands. Crucially, the devices operate in the visible range (RGB), essential for retina-inspired color sensing, demonstrating inhibitory postsynaptic current (IPSC) behavior under 450, 550 and 740 nm illumination. A low power consumption of ~40 nJ was also recorded under red light illumination. The system successfully emulates fundamental synaptic behaviors including paired-pulse depression (PPD), spiking-number-dependent plasticity (SNDP), and spiking-rate-dependent plasticity (SRDP), enabling biologically plausible visual processing.

The use of light into the design of optoelectronic memristors has lately garnered significant attention, emerging as a leading frontier in neurosynaptic device research.[1] Since over 70% of human sensory information is derived from vision, the integration of light-stimulated optoelectronic synapses into artificial neural networks (ANNs) offers a cutting-edge platform for emulating the biological visual perception system and realizing neuromorphic biomimetic functionalities.[1,2] To overcome the limitations of conventional computer architectures, photonic solutions for processing have evolved, offering a promising approach for enhanced computational performance.[3] To this end, the development of robust optical synapses is considered of great importance.

Although the excitation of optical synapses with light pulses has been reported in many works in the literature[4–6], the inhibition remains a challenge and in most of the cases complex material configurations are used.[7–14] Optical inhibition is particularly crucial in retinal-inspired neuromorphic systems, where it emulates the role of $GABA_A$ receptors in regulating lateral and feedback inhibition.[15] This mechanism enables precise control over synaptic weight modulation in memristive devices, enhancing both network stability and adaptive information processing. Inhibitory synapses can generally be engineered to exhibit dynamic, tunable inhibition by adjusting light intensity, wavelength, or phase, mimicking the plasticity seen in biological systems.[16,17] By enabling fast and energy-efficient inhibitory control, optoelectronic synapses hold promise for advancing real-time processing in applications, such as autonomous robotics, brain-computer interfaces, and sensory data interpretation.[18]

In this work, low power optoelectronic inhibitory synapses from ultra small nanocrystal arrays, namely lead sulfide (PbS), were fabricated and systematically examined. PbS is a common material, used for solar cells[19], photodetectors[20], transistors[21,22] and memristors [23,24]. The fabricated synapses were irradiated with optical pulses in the visible (RGB) range and a fully optical control of the synapse inhibition state was achieved. Our work provides valuable insights for the future fabrication of scalable artificial neural networks with accurate optoelectronic control of their synaptic properties.

Although the synthesis of PbS quantum dots (QDs) has been extensively studied and evolved for decades[25–27], their application into functional optoelectronic devices remains challenging. The most widely employed method for the synthesis of high quality QDs is the hot-injection reaction at an elevated temperature, where long aliphatic molecules (e.g., oleic acid, oleylamine, etc) are used as surface ligands to control the nucleation and growth. Although these ligands are

---

[a] School of Applied Mathematical and Physical Sciences, National Technical University of Athens, 15780 Athens, Greece. E-mail: chryssipanagopoulou@mail.ntua.gr
[b] Institute of Nanoscience and Nanotechnology, NCSR Demokritos, 15341, Athens, Greece. E-mail: t.stergiopoulos@inn.demokritos.gr
[c] Department of Chemistry, National and Kapodistrian University of Athens, 15772 Athens, Greece.

View Article Online
DOI: 10.1039/D5TC03487F

mandatory to produce high quality monodisperse QDs, they function as electrically insulating media hence hindering carrier transport in QD-based optoelectronic devices. To solve this problem, post-synthetic ligand-exchange strategies have been proposed to substitute the bulky ligands with shorter, more conductive ones. However, efficient ligand exchange in colloidal PbS QDs remains a challenge due to the Pb-Olate bond cleavage that usually leads to the formation of trap states.[28] Recently, a direct synthetic approach was developed by the Ma group.[29–32] This method completely circumvents the ligand exchange process and instead leverages an in-situ surface passivation of the QD with iodide species. The final QDs are dispersed in polar solvents and offer superior efficiency.

The synthesis of PbS nanoparticles followed previous reports with adaptations.[29,33] In a nitrogen filled glovebox, 4mmol of lead iodide (PbI_2, TCI, 99.99%) were dissolved in 5mL of N,N-Dimethylformamide (DMF, Thermo Fisher Scientific, 99%). To facilitate the dissolution the mixture was heated at 100°C until a transparent yellow solution was obtained. Then, the solution was cooled down to room temperature and added to 1mmol of N,N'-Diphenylthiourea (DPTU, Thermo Fisher Scientific, 98%). The final solution was stirred at room temperature for 2 minutes and then 0.4mL of n-Butylamine (Thermo Fisher Scientific, 99+%) was swiftly injected, instantly forming a black colloid. The colloid was left to stir for 10 minutes before adding an excess amount of toluene (anhydrous, Thermo Fisher Scientific, 99.8%) (4:1) to precipitate the nanoparticles and consequently centrifuged for 10 minutes at 6000 rpm to collect the solids. The solids were dried under vacuum and then redispersed in DMF with a concentration of 200 mg/mL for device fabrication.

Transmission electron microcopy (TEM) images showed uniformly dispersed nanocrystals with an average size of 2.5–3 nm (Fig. 1c), indicative of strong quantum confinement. X-ray photoelectron spectroscopy (XPS) analysis (Fig. 1d) confirmed the presence of iodide through the I3d spectrum (iii), while the Pb4f (i) and S2p (ii) spectra verified the chemical composition and oxidation states consistent with PbS. The presence of iodine peaks indicates successful ligand exchange and surface passivation.[35] The X-ray diffraction (XRD) patterns (Fig. 1e) exhibited sharp peaks corresponding to the face-centered cubic phase of PbS, with no impurity phases detected. These results confirm the successful ligand exchange, high crystallinity, and structural purity of the QDs, making them promising for optoelectronic applications.

Interdigitated Ti (7 nm)/Au (75 nm) electrodes with a 10 µm gap were fabricated on top of Si/SiO_2 (300 nm) substrates (Fig. S1b), using standard optical lithography and lift-off processes. The PbS layer was deposited by spin-coating PbS-I dispersion in DMF (200mg/ml) at 4000 rpm and dried in air at 70°C for 5 minutes. The samples were measured by profilometry to have a thickness of approximately ~350 nm, which is in good agreement with values reported in the literature. [34] Fig. 1a depicts the structure of the PbS NCs capped with iodide ligands; a schematic illustration of our device can be seen in Fig. 1b. The electrical measurements were conducted using a Keithley 4200-SCS semiconductor parameter analyzer. The triggering of the power LED array was conducted using the HP 8116A Pulse Generator.

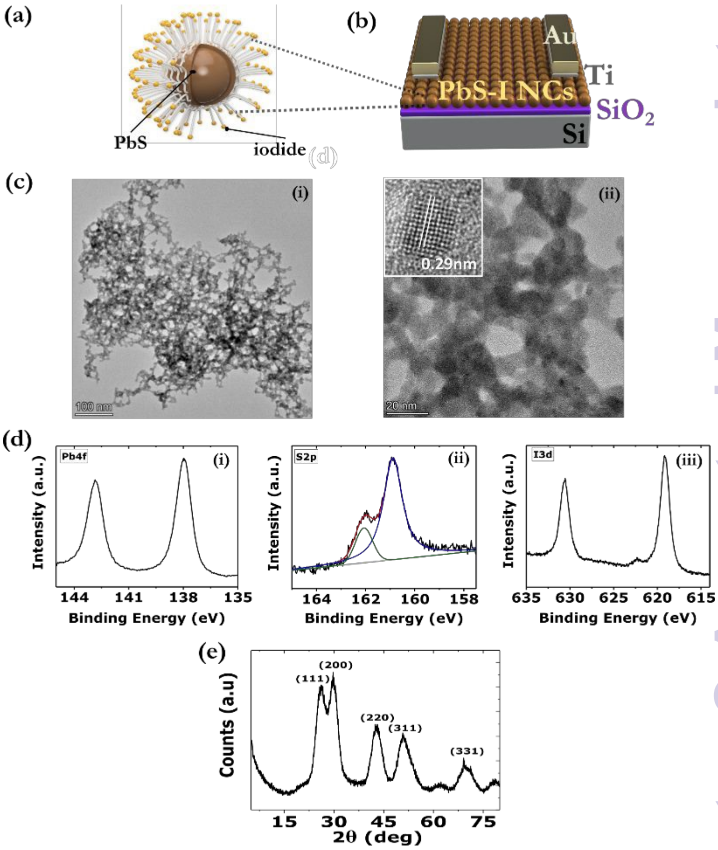

Fig. 1. Schematic illustration of (a) PbS with iodide ligands and (b) the fabricated device. (c) TEM plan view image of the PbS nanocrystals. The scale bar in (i) corresponds to 100 nm and to 20 nm in (ii). The inset shows a high-resolution image of a NC. (d) Pb4f (i), S2p (ii) and I3d (iii) XPS spectra of PbS-I films with the corresponding peaks after fitting analysis. (e) XRD diffractogram of PbS.

Fig. 2a demonstrates the inhibitory postsynaptic current (IPSC) in response to a single 20 s optical pulse at wavelengths of 450 nm, 550 nm and 740 nm. As the wavelength increases, the photocurrent progressively decreases. This is because the photon energy diminishes with increasing wavelength, reducing the likelihood of electronic transitions across the energy bandgap. Additionally, the optical absorption coefficient generally decreases with wavelength, further contributing to the decline in photocurrent[36]; this is also illustrated in the absorbance spectrum of Fig. S2. A shift from short-term memory (STM) to long-term memory (LTM) occurs with higher pulse width (Fig. 2b, c), as well as with increased pulse number (Fig. 2d-f), indicating the successful mimicking of the spike-width dependent plasticity (SWDP) and spike-number dependent plasticity (SNDP) of the proposed synaptic device [37]. The post pulse current of Fig. 2b was also fitted with a decay function, which lead to the decay exponent increasing its value from 8.2 for the 1 s pulse to 27 for the 20 s optical pulse; thus, the STM to LTM was verified.

Paired-pulse depression (PPD) is a key synaptic plasticity property, characterized by a neurotransmitter-induced

View Article Online
DOI: 10.1039/D5TC03487F

reduction in action potential, that serves as an important indicator of information processing at biological synapses. PPD behavior can be demonstrated by delivering two consecutive identical light pulses, with the second pulse eliciting a stronger inhibitory response than the first. The PPD index, defined as

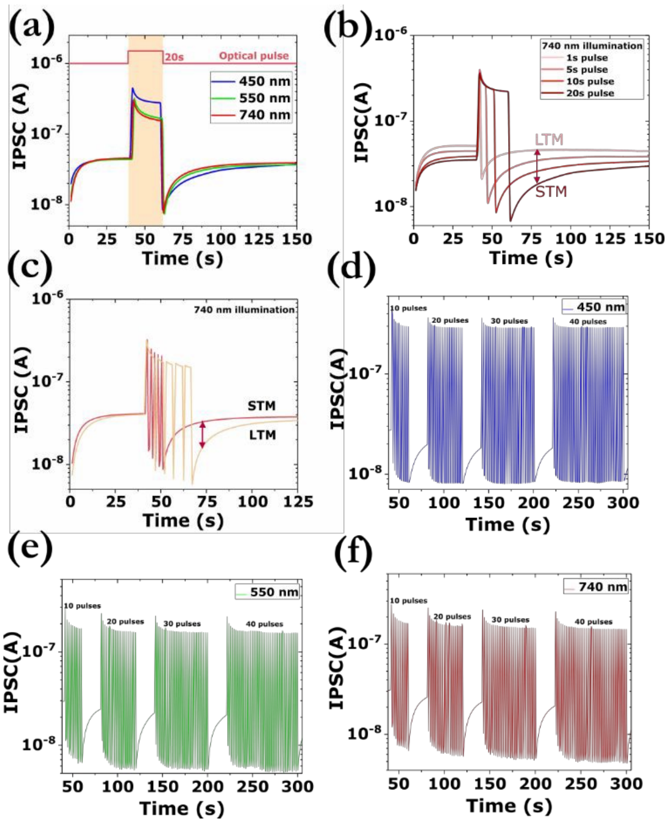

Fig. 2. (a) IPSC response induced by a presynaptic optical pulse with a duration of 20 s for three different wavelengths with the same intensity of 1.22 mW/cm^2. (b) Transition from STM to LTM under the application of single optical pulses with increasing duration for illumination of 740 nm. (c) Impact of the pulse width on LTM to STM transition for 740 nm irradiation. The red line corresponds to 5 pulses of 1 s width, while the yellow one refers to five 5 s-pulses. All IPSC responses were recorded at a read-out voltage of 1 V. (d-f) IPSC triggered by stimulus trains with different pulse numbers for three distinct wavelengths; 450 (d), 550 (e) and 740 nm (f) (frequency: 1 Hz, duration: 1 s).

$$PPD = \frac{A_2}{A_1} \times 100\% \qquad (1)$$

(where A_1 and A_2 are IPSC amplitudes for the first and second pulses, respectively, inset Fig. 3a) increased from 55.1% to 93.4% as the interstimulus interval (Δt) extended from 1 s to 40 s, as seen in Fig. 3a for 740 nm irradiation. Fig. 3a (inset) illustrates PPD for paired 10 s pulses at Δt = 20 s. The dependence on the time interval follows a mono-exponential function[38]:

$$PPD = C_1 \exp(-t/\tau) \qquad (2)$$

where C_1 is a fitting constant, and τ represents the relaxation time associated with this effect. From our analysis, the relaxation times was estimated to be 10.4 s, which is comparable to the response times observed in biological synapses.[39] Similar graphs can be seen in Fig. S3 for 450 and 550 nm illumination, along with the corresponding fitting analysis.

Another key characteristic of optoelectronic memristors lies in their capacity to modulate synaptic weight (conductance or resistance) in response to the intensity and frequency of incoming optical or electrical stimuli.[1] The synaptic weight change (SWC), defined as

$$SWC = \frac{A_n - A_1}{A_1} \times 100\% \qquad (3)$$

was used to evaluate this synaptic property, with A_n and A_1 denoting the final and initial synaptic current values for four distinct optical frequencies, respectively [12]. Figure 3b illustrates the variation of SWC with spike frequency, revealing that higher frequencies lead to a more pronounced inhibitory response. The SRDP behavior of the device indicates that high-repetition training can enhance brain-like forgetting capabilities[5] and enable low-pass filtering for signal processing.[39,40] Specifically, the increase of the optical pulse frequency from 1 to 4 Hz reduced the synaptic weight from approximately −48.1% to −72.5% under 550 nm light irradiation (Fig. 3b).

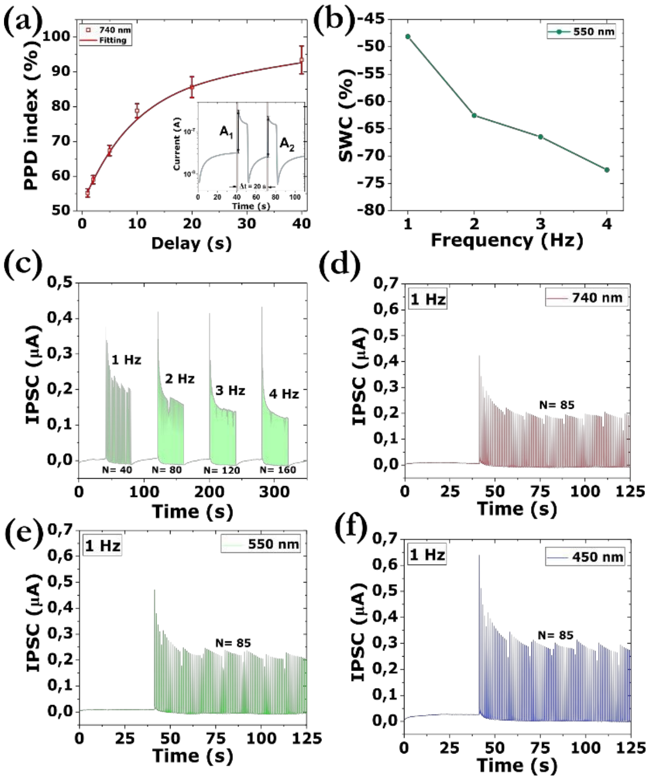

Fig. 3. (a) Distribution of the PPD index as a function of the pulse interval (Delay Δt) of the optical pulses. (b) The plot of synaptic weight via the pulse frequency for 550 nm light illumination (pulse width: 200 ms, intensity: 1.22 mW/cm^2). (c) IPSC triggered by 4 consecutive trains of light pulses with different pulse frequencies (wavelength: 550 nm, duration: 200 ms) on a linear scale. *N* denotes the number of light pulses. (d-f) IPSC triggered by stimulus trains with three distinct wavelengths on a linear scale; 740 (d), 550 (e) and 450 nm (frequency: 1 Hz, duration: 200 ms, intensity: 1.22 mW/cm^2). *N* refers to the number of light pulses.

Further validation is depicted in Fig. 3c, where synaptic event frequency was elevated when optical pulse frequency was increased from 1 to 4 Hz. Additional graphs of the SWC for red and blue irradiation are illustrated in Fig. S4.

The 450 nm optical pulse induced larger IPSC amplitudes compared to 550 and 740 nm stimulation, with synaptic weight

View Article Online
DOI: 10.1039/D5TC03487E

changes exhibiting consistent wavelength-dependent trends. The same pattern held true under the application of a train of pulses with a duration of 200 ms, as illustrated in Fig. 3d-f, for a 1 Hz optical pulses' frequency, as well as for shorter optical pulses of 100 ms (Fig. 4). In Fig. S5 the synthesis of PbS QDs via the hot-injection reaction with oleic acid (OA) shows no photoresponse during the irradiation of 450 nm light under the same conditions, verifying the insulating nature of these ligands. A low average energy consumption per spike of 40 nJ for red, 50 nJ for green and 55 nJ for blue light irradiation was calculated based on the following equation:

$$E_{spike} = V \times I \times t_{spike} \qquad (4)$$

where the V is the voltage drop across the memristor (1 V), I is the current of the generated spikes (~0.4 μA for 740 nm, ~0.5 μA for 550 nm and ~0.55 μA for 450 nm illumination) and t_{spike} is their width (~100 ms).

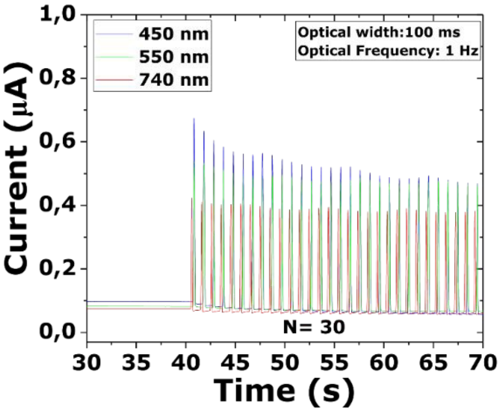

Fig. 4. IPSC triggered by stimulus trains with three distinct wavelengths on a linear scale. The optical frequency of the irradiation was 1 Hz, while the optical width of the pulses was set to 100 ms. For all three wavelengths, the optical intensity was measured to be 1.22 mW/cm^2. *N* refers to the number of light pulses.

To understand the origins of the optoelectronic inhibitory behavior of our synaptic devices, we conducted ultraviolet photoelectron spectroscopy (UPS) characterization (Fig. 5a), based on which the energy band diagram of the PbS NCs–Au electrodes was constructed (Fig. 5b). Under RGB illumination, PbS NCs exhibit a characteristic photoresponse where initial photoexcitation generates excitons that dissociate into free carriers, producing a rapid current spike [41,42]. Despite iodide passivation, residual traps (e.g., sulfur vacancies and electron trapping sites of silanol on the SiO_2 surface) can capture photogenerated electrons over time with a higher rate than the photoexcitation [43–46]; the initial peak current subsequently decays due to progressive trap-state filling, eventually reaching a steady-state balance between continuous carrier generation and trap-mediated losses. The observed decay time is attributed to the RC charging dynamics of the system, where the PbS NC network functions as a distributed capacitor, and a parallel resistive pathway models the leakage current between the electrodes through the percolating NC network. To quantitatively capture this behavior, the electrical response was modeled using a first-order resistor–capacitor (RC) circuit (LTspice), which reproduces the exponential charging and discharging dynamics (Fig. 5c); the agreement between experimental and simulated data under a 10 s optical pulse (740 nm) is shown in Fig. 5d. Although the nanocrystals exhibit strong quantum confinement with discrete energy levels, the equivalent RC circuit is employed as a phenomenological model to describe the macroscopic electrical relaxation behaviour. In particular, the first-order RC model effectively describes the charging and discharging dynamics of the nanocrystal ensemble as a whole, averaged over a large number of confined domains. Under small-bias and near-equilibrium conditions, the device shows a quasi-linear current–voltage response, justifying the use of a first-order linear approximation. The extracted RC parameters therefore represent the averaged charge transport and storage dynamics across the nanocrystal network, rather than the microscopic nonlinearities of individual confined states.

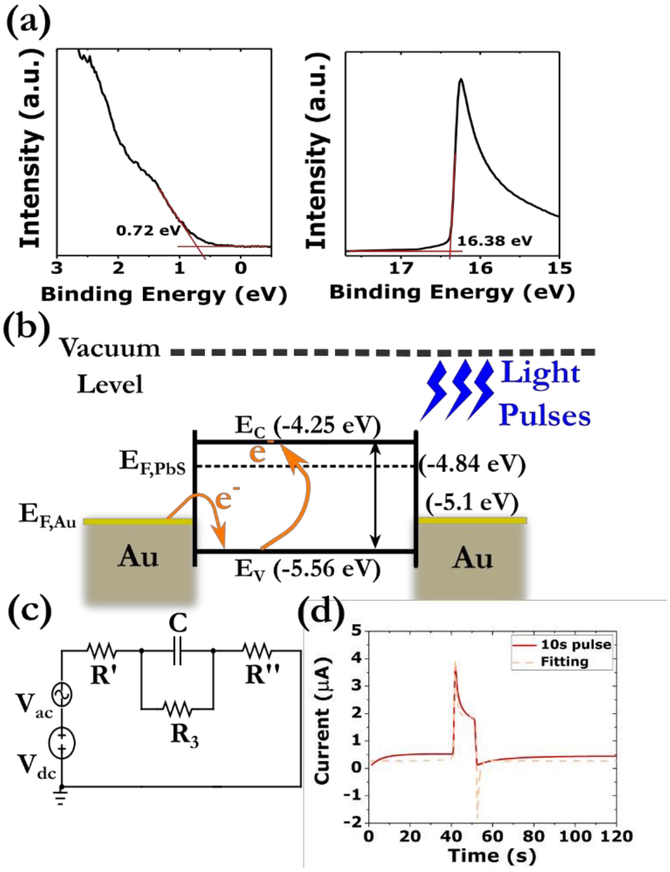

Fig. 5. (a) UPS spectra of PbS film. (b) Energy band diagram of the PbS NCs-Au electrodes. (c) Equivalent circuit of the proposed device, which consists of the capacitance of the PbS NC network, connected in parallel to resistance R_3 of the iodide ligands between the QDs. Gold electrodes are modeled as $R'=R_1+R_{contact}$ and $R''=R_2+R_{contact}$, each equal to 6 MΩ. The electrode resistances reflect both the intrinsic series resistance of the interdigitated gold fingers (which is negligible) and the metal/semiconductor contact resistance. These values provide a realistic representation of the baseline device conductance prior to optical excitation and were used to define accurate boundary conditions for the circuit simulations. In the hybrid electro-optical setup, a V_{dc} bias of 1 V was applied electrically, while optical inputs were simulated as modulated pulses with an effective AC amplitude. During charging (irradiation V_{dc}= 1 V and V_{ac}=6 V were applied; during discharging, only the DC bias was maintained. The extracted capacitance value was 200 nF, and R_3 was calculated as 25 MΩ. (d) Fitting between experimental (10 s pulse duration at 740 nm) and simulation data, according to the equivalent circuit model.

When the light is turned off, the current initially drops rapidly as photoexcitation ceases, reaching a minimum value as

View Article Online
DOI: 10.1039/D5TC03487F

trapped charges effectively screen the internal electric field, particularly at the PbS/SiO_2 interface where holes tend to accumulate due to the insulating nature of the substrate. The subsequent exponential recovery of the current toward its initial dark current level, also denoted as the capacitive discharging time, is driven by the thermal release of trapped charges. Over time, carriers escape from shallow trap states through a thermally activated process, with the timescale governed by the trap depth and temperature according to an Arrhenius relationship.[47,48] Simultaneously, charges accumulated at the PbS/SiO_2 interface slowly leak back into the quantum dot layer, while the Schottky barrier at the Au/PbS contacts gradually relaxes as the screening effects diminish. This recovery process typically occurs on millisecond to second timescales, depending on the quality of the quantum dot passivation and the specific interface properties [49].

Conclusions

In conclusion, this work tackles the key challenge of developing an optoelectronic inhibitory synapse tailored for the maintenance of excitation–inhibition balance within artificial neural circuits. We analysed the behavior of the device, which was based on lead sulfide (PbS) NCs capped with iodide ligands, in the visible range by implementing different synaptic schemes, such as PPD and SRDP, while achieving a low energy consumption in the range of 40-55 nJ. By harnessing interfacial chemistry at the nanocrystal level, we demonstrate a pathway to optoelectronic synapses that unite efficiency, tunability, and scalability, while also exhibiting a simple configuration scheme. In contrary to previously reported devices in the literature, our optoelectronic synapse achieved optical inhibition in three wavelengths of the retinal spectrum (RGB) (Table S1). This strategy opens new horizons for neuromorphic platforms, where chemical design principles directly dictate technological reach at the forefront of neuromorphic computing for autonomous systems with real-time sensory processing.

Author contributions

Conceptualization: C. P., P. B., T. S. and D. T. Methodology: C. P., P.B., A. K., S. O., C.T., A. B., P. T., A. G. K. Formal analysis and data curation: C. P., P. B., A. K., S. O. and C.T. Writing—original draft preparation, C.P., P. B., A. K. and S. O. Writing—review and editing, C. P., P. B., A. K., S. O., T.S. and D.T. Supervision: A.G. K., T. S and D.T.

Conflicts of interest

There are no conflicts to declare.

Data availability

The data that support the findings of this study are available from the corresponding author upon reasonable request.

Acknowledgements

Four of the authors (C. P., P. B, C. T., D. T.) would like to acknowledge financial support for this work from the EU project ELEGANCE funded by the European Innovation Council and SMEs Executive Agency. This project has received funding from the HORIZON-EIC-2023-PATHFINDERCHALLENGES-01 call under grant agreement No 101161114.

S. O. and T. S. would like to acknowledge financial support from the European Research Council (ERC) through the Consolidator Grant (818615-MIX2FIX). The work of S. O. has been also financially supported by the Hellenic Foundation for Research and Innovation (HFRI) under the 5th Call for HFRI PhD Fellowships (Fellowship Number:19304).

References

1 J. Wang, N. Ilyas, Y. Ren, Y. Ji, S. Li, C. Li, F. Liu, D. Gu and K.-W. Ang, *Advanced Materials*, 2024, **36**, 2307393.
2 R. Khan, N. Ur Rahman, M. Faisal Hayat, D. Ghernaout, A. A. M. Salih, G. Abbas Ashraf, A. Samad, M. Adil Mahmood, N. Rahman, M. Sohail, S. Iqbal, S. Abdullaev and A. Khan, *Nanoscale*, 2024, **16**, 14589–14620.
3 R. Li, Y. Gong, H. Huang, Y. Zhou, S. Mao, Z. Wei and Z. Zhang, *Advanced Materials*, 2025, **37**, 2312825.
4 W. Zhou, R. Yang, H.-K. He, H.-M. Huang, J. Xiong and X. Guo, *Applied Physics Letters*, 2018, **113**, 061107.
5 Y.-X. Hou, Y. Li, Z.-C. Zhang, J.-Q. Li, D.-H. Qi, X.-D. Chen, J.-J. Wang, B.-W. Yao, M.-X. Yu, T.-B. Lu and J. Zhang, *ACS Nano*, 2021, **15**, 1497–1508.
6 S. Cho, S. S. Kundale, J. Shim, S. Park, H. Kwak, A. V. Hoang, E.-T. Kim, S. Kim and J. H. Park, *ACS Appl. Mater. Interfaces*, 2025, **17**, 6460–6472.
7 C.-M. Yang, T.-C. Chen, D. Verma, L.-J. Li, B. Liu, W.-H. Chang and C.-S. Lai, *Advanced Functional Materials*, 2020, **30**, 2001598.
8 S. W. Cho, S. M. Kwon, Y.-H. Kim and S. K. Park, *Advanced Intelligent Systems*, 2021, **3**, 2000162.
9 Z. Shen, C. Zhao, L. Kang, Y. Sun, Y. Liu, I. Z. Mitrovic, L. Yang, E. G. Lim, Z. Zeng and C. Zhao, *Advanced Intelligent Systems*, 2022, **4**, 2100236.
10 D. Rao, A. I. K. Pillai, M. Garbrecht and B. Saha, *Advanced Electronic Materials*, 2023, **9**, 2200975.
11 M. Cui, P. Zhao, C. Jiang, B. Tian, C. Luo, H. Lin, H. Peng and C.-G. Duan, *ACS Applied Electronic Materials*, 2023, **5**, 3403–3409.
12 C. Zhu, T. Guo, H. Zhang, J. Jiang, Z. Lin, X. Wei, L. Wang, X. Liu, X. Li, X. Yu and W. Huang, *Journal of Materials Chemistry C*, DOI:10.1039/D5TC01522G.
13 R. Yang, D. Hu, Q. Chen, Z. Wang, B. Lu, Z. Ye, X. Li and J. Lu, *Advanced Functional Materials*, 2025, **35**, 2414210.
14 W. Huang, S. Jiang, Z. Lin, X. Zhang, H. Fei, J. Jiang, J. Tang, X. Zhang, X. Yu and L. Wang, *Applied Physics Reviews*.
15 J. Nagy, B. Ebbinghaus, M. Hoon and R. Sinha, *eLife*, 2021, **10**, e60994.
16 S. Ebert, T. Buffet, B. S. Sermet, O. Marre and B. Cessac, *Nat Commun*, 2024, **15**, 6118.
17 F. Zhang, C. Li, Z. Li, L. Dong and J. Zhao, *Microsyst Nanoeng*, 2023, **9**, 16.
18 Y. Kim, C. W. Lee and H. W. Jang, *J. Electron. Mater.*, 2025, **54**, 3609–3650.
19 Y. Cao, A. Stavrinadis, T. Lasanta, D. So and G. Konstantatos, *Nat Energy*, 2016, **1**, 16035.

View Article Online
DOI: 10.1039/D5TC03487F

20 F. Fang, Y. Tang, H. Tang, Y. Song, Q. Chen, L. Rao, S. Xiao, W. Chen and L. Cao, *ACS Appl. Electron. Mater.*, 2025, **7**, 7368–7376.

21 K. Shibata, M. Yoshida, K. Hirakawa, T. Otsuka, S. Z. Bisri and Y. Iwasa, *Nat Commun*, 2023, **14**, 7486.

22 T. Feng, H. Xu, Y. Yang, X. Hu, T. Wang, H. Zhu, Q. Sun, D. W. Zhang, J. Meng and L. Chen, *Nano Lett.*, 2025, **25**, 3637–3645.

23 J. Lin, Z. Wang, Q. Lin, J. Sun, X. Guo, Y. Wang, L. Lin, Y. Zhao, Y. Liu and D. Li, *The Journal of Physical Chemistry Letters*, 2024, **16**, 199–208.

24 X. Lin, Z. Lin, W. Zhao, S. Xu, E. Chen, T. Guo and Y. Ye, *Applied Physics Letters*, 2025, **126**, 263503.

25 M. A. Hines and G. D. Scholes, *Advanced Materials*, 2003, **15**, 1844–1849.

26 B. Yuan, T. K. Egner, V. Venditti and L. Cademartiri, *Nature Communications*, 2018, **9**, 1–7.

27 C. Ding, D. Wang, D. Liu, H. Li, Y. Li, S. Hayase, T. Sogabe, T. Masuda, Y. Zhou, Y. Yao, Z. Zou, R. Wang and Q. Shen, *Advanced Energy Materials*, DOI:10.1002/aenm.202201676.

28 M. Liu, O. Voznyy, R. Sabatini, F. P. García de Arquer, R. Munir, A. H. Balawi, X. Lan, F. Fan, G. Walters, A. R. Kirmani, S. Hoogland, F. Laquai, A. Amassian and E. H. Sargent, *Nature Materials*, 2017, **16**, 258–263.

29 Y. Wang, Z. Liu, N. Huo, F. Li, M. Gu, X. Ling, Y. Zhang, K. Lu, L. Han, H. Fang, A. G. Shulga, Y. Xue, S. Zhou, F. Yang, X. Tang, J. Zheng, M. Antonietta Loi, G. Konstantatos and W. Ma, *Nature Communications*, 2019, **10**, 5136.

30 Y. Liu, Y. Gao, Q. Yang, G. Xu, X. Zhou, G. Shi, X. Lyu, H. Wu, J. Liu, S. Fang, M. I. Ullah, L. Song, K. Lu, M. Cao, Q. Zhang, T. Li, J. Xu, S. Wang, Z. Liu and W. Ma, *Angewandte Chemie - International Edition*, DOI:10.1002/anie.202300396.

31 L. Yuan, Y. Li, Y. Liu, K. Lu, G. Shi, X. Sun, Y. Li, X. Dong, Y. Xiao, L. Huang, Z. Liu and W. Ma, *Angewandte Chemie - International Edition*, DOI:10.1002/anie.202416369.

32 X. Ding, X. Wen, Y. Kawata, Y. Liu, G. Shi, R. ben Ghazi, X. Sun, Y. Zhu, H. Wu, H. Gao, Q. Shen, Z. Liu and W. Ma, *Nanoscale*, 2024, **16**, 5115–5122.

33 Y. Liu, Y. Gao, Q. Yang, G. Xu, X. Zhou, G. Shi, X. Lyu, H. Wu, J. Liu and S. Fang, *Angewandte Chemie International Edition*, 2023, **62**, e202300396.

34 Y. Liu, Y. Gao, Q. Yang, G. Xu, X. Zhou, G. Shi, X. Lyu, H. Wu, J. Liu and S. Fang, *Angewandte Chemie International Edition*, 2023, **62**, e202300396.

35 Y. Wang, Z. Liu, N. Huo, F. Li, M. Gu, X. Ling, Y. Zhang, K. Lu, L. Han, H. Fang, A. G. Shulga, Y. Xue, S. Zhou, F. Yang, X. Tang, J. Zheng, M. Antonietta Loi, G. Konstantatos and W. Ma, *Nat Commun*, 2019, **10**, 5136.

36 H. Wu, Z. Liu, B. Wang, L. Zheng, S. Lian, J. Zhang, S. Zhang, G. Zhang, Z. Xue, S. Yang, X. Cheng, G. Ding, Z. Liu, C. Ye and G. Wang, *ACS Photonics*, 2024, **11**, 1342–1351.

37 S. G. Kim, Q. Van Le, J. S. Han, H. Kim, M.-J. Choi, S. A. Lee, T. L. Kim, S. B. Kim, S. Y. Kim and H. W. Jang, *Advanced Functional Materials*, 2019, **29**, 1906686.

38 R. S. Zucker and W. G. Regehr, *Annual review of physiology*, 2002, **64**, 355–405.

39 L. F. Abbott and W. G. Regehr, *Nature*, 2004, **431**, 796–803.

40 B. Chen, S. Sun, S. Fan, X. Liu, Q. Li and J. Su, *Advanced Electronic Materials*, 2022, **8**, 2200864.

41 I. Ka, V. Le Borgne, K. Fujisawa, T. Hayashi, Y. A. Kim, M. Endo, D. Ma and M. A. El Khakani, *Sci Rep*, 2016, **6**, 20083.

42 J. Gao and J. C. Johnson, *ACS Nano*, 2012, **6**, 3292–3303.

43 Z. Jin, A. Wang, Q. Zhou, Y. Wang and J. Wang, *Sci Rep*, 2016, **6**, 37106.

44 J. Hu, X. He, H. Pu, Y. Yang and C. Chen, *Superlattices and Microstructures*, 2020, **145**, 106616.

45 A. A. Bakulin, S. Neutzner, H. J. Bakker, L. Ottaviani, D. Barakel and Z. Chen, *ACS Nano*, 2013, **7**, 8771–8779.

46 M. I. Nugraha, R. Häusermann, S. Z. Bisri, H. Matsui, M. Sytnyk, W. Heiss, J. Takeya and M. A. Loi, *Advanced Materials*, 2015, **27**, 2107–2112.

47 H. Zhao, H. Liang, F. Vidal, F. Rosei, A. Vomiero and D. Ma, *J. Phys. Chem. C*, 2014, **118**, 20585–20593.

48 G. Konstantatos and E. H. Sargent, *Applied Physics Letters*, 2007, **91**, 173505.

49 V. Gray, J. R. Allardice, Z. Zhang, S. Dowland, J. Xiao, A. J. I. Petty, J. E. Anthony, N. C. Greenham and A. Rao, *ACS Nano*, 2020, **14**, 4224–4234.

View Article Online
DOI: 10.1039/D5TC03487F

Data Availability Statement

Data for this article, including XPS, XRD, TEM and UPS characterization, as well as optoelectronic characterization, are available at Open Science Framework repository, under the title “Low power optoelectronic inhibitory synapses in the visible range from PbS nanocrystal arrays” and identifier: DOI 10.17605/OSF.IO/RW6Y3.